Earthq Eng & Eng Vib (2019) 18: 255-266 **DOI**: https://doi.org/10.1007/s11803-019-0502-0

Scattering and reflection of SH waves around a slope on an elastic wedged space

Liu Qijian[1†], Wu Zhiyu[1‡] and Vincent W Lee[2§]

1. *College of Civil Engineering, Hunan University, Changsha 410082, China*

2. *Civil and Environmental Engineering, University of Southern California, Los Angeles 90089, United States*

Abstract: The scattering and reflection of SH waves by a slope on an elastic wedged space is investigated. A series solution is obtained by using the wave function expansion method. The slope on a wedged space is divided into two sub-regions by an artificial, auxiliary circular arc. The wave fields with unknown complex coefficients within each sub-region are derived. Applying Graf addition theorem, the scattered waves in the sub-regions are expressed in a global coordinate system. Fourier transform is adopted to derive a consistent form of standing waves in the inner region using the orthogonality of the cosine functions. The boundary-valued problem is solved by stress and displacement continuity along the artificial, auxiliary arc to obtain the unknown complex coefficients. Parametric studies are next performed to investigate how the topography from the slope on the wedged space will affect the scattering and diffraction, and hence the amplification and de-amplification of the SH waves. Numerical results show that the surface motions on the slope of the wedged space is influenced greatly by the topography. Amplification of the surface motions near the slope vertex is significant. The corresponding phases along the wedged space surfaces are consistent with the direction that the SH waves are propagating.

Keywords: earthquake ground motion; wave scattering and diffraction; Graf addition theorem; Fourier transform

1 Introduction

Scattering and diffraction take place as seismic waves propagate in the medium with irregular topographies, such as canyon, valley, convex form and slope. Amplification or de-amplification is observed when the wavelengths of the seismic waves are comparable to the dimensions of the irregular topographies. Such phenomenon of the topographic effect was first observed at a site on a sharp ridge near the Pacoima Dam abutment during the San Fernando earthquake (Trifunac, 1971). Then, the topographic effect of the seismic waves has drawn great attention from many researchers through seismic records and site investigations (Trifunac and Hudson, 1971; Aboudi, 1971; Boore, 1972, Bouchon, 1973; Abo-Zena and King, 1973; Bard, 1982; Geli 1988; Sánchez-Sesma and Campillo, 1991; Hartzell *et al.*, 1994; Fu, 2005; Hough *et al.*, 2010).

To understand and reveal the nature of topographic effect of seismic waves, various methods have been proposed such as the finite element method, boundary element method and analytical solutions. The finite element method can be applied to complex media and irregular geometry. However, an artificial boundary is needed to truncate the infinite space as a finite one (Smith, 1975; Shah *et al.*, 1982; Zhang and Zhao, 1988). Thus, the Sommerfeld's radiation condition can't be satisfied exactly. Moreover, verification and calculation efficiency are the key problem for numerical implementation. Compared to the finite element method, boundary element method satisfies automatically the Sommerfeld's radiation condition by using the fundamental solution (Wong and Jennings, 1975; Sills, 1978; Sánchez-Sesma and Rosenblueth, 1979; Luzón *et al.*, 1997; Takemiya and Fujiwara, 1994; Bouchon and Sánchez-Sesma, 2007; Sohrabi-Bidar *et al.*, 2010; Alielahi *et al.*, 2015). However, considerable computation efforts need to be performed during the calculation process.

As for analytical solutions, the wave function expansion method is mathematically rigorous and easy to be applied to the scattering of waves by simple topographies. It can also reveal the nature of diffraction of seismic wave by topography and be served as a benchmark to the numerical methods. By using the wave function expansion method, Trifunac investigated the scattering of plane SH waves by a semi-cylindrical canyon (Trifunac, 1973). Many researches have been accomplished for scattering of seismic waves by various topographies such as a semi-cylindrical hill (Yuan and

Correspondence to: Vincent W Lee, Civil and Environmental Engineering, University of Southern California, 3620 S Vermont Ave KAP210 CEE m/c2531 Los Angeles, CA 90089, United States
Tel: +1-213-7400568
E-mail: vlee@usc.edu
[†]Associate Professor; [‡]Graduate student; [§]Professor
Received March 12, 2018; **Accepted** August 25, 2018

Men, 1992; Zhang et al, 2018), a cylindrical canyon of the circular-arc cross section (Yuan and Liao, 1994), a cylindrical hill of the circular-arc cross section (Yuan and Liao, 1996, Lee *et al.*, 2006), a convex circular arc (Tsaur and Chang, 2009), a V-shaped canyon of various type (Tsaur and Chang, 2008; Tsaur *et al.*, 2010; Zhang *et al.*, 2012; Gao and Zhang, 2013; Chang *et al.*, 2015), a U-shaped canyon (Gao *et al*. 2012), and a trapezoidal valley with a circular-arc alluvium (Zhang *et al.*, 2015), a shallow rectangular cavity (Liu *et al.*, 2016). Generally, method of the auxiliary circle and Graf's addition theorem are useful tools to formulate the solution of the boundary-valued problem.

The above researches all use the polar coordinate system in the determination of the scattered wave fields involving the circular arc or circle. However, for some other special topographies, it is also convenient to use other coordinate system. For example, curvilinear orthogonal coordinate (Lamé, 1859, Jeffery, 1921, Love, 1944) can be used for some other special topographies, such as a semielliptical canyon (Wong and Trifunac, 1974), a semi-parabolic cylindrical canyon (Lee, 1990), a lower semielliptical convex (Tsaur, 2011), a concentric elliptical tunnel (Amornwongpaibun *et al.*, 2016). In addition, the complex function method is also a very powerful tool in the scattering of waves (Liu *et al.*, 1982; Liu and Han, 1991; Liu *et al.*, 2010; Liu *et al.*, 2016; Zhang *et al.*, 2017).

It is found that the solution for the scattering of seismic waves by a slope on an elastic wedged space has not yet been studied. The slope on a wedged space, or the 3-sided wedge, can be generalized from the slope with a cut. This kind of topography is very common in geophysics and geotechnical engineering. Many investigations have been conducted for the scattering of waves by a wedge space. MacDonald, in a book (Macdonald, 1902), expressed the total electromagnetic field in a wedge medium in terms of Bessel functions, from which Sánchez-Sesma used the same functions to study the scattering of SH waves by a wedge (Sánchez-Sesma, 1985). The Bessel functions of non-integer order were used to automatically satisfy the traction-free boundary condition. Lee and Sherif derived the diffraction of SH waves by a circular canyon in an elastic wedged space (Lee and Sherif, 1996; Sherif and Lee, 1996). In this study, the scattering and reflection of SH waves by a slope on a wedged space is investigated analytically by using the Graf addition theorem and Fourier transform technique.

2 The Mathematical model and formulation

2.1 The model

The model of interest is shown in Fig. 1. The slope on a wedged space is enclosed by two half lines *AD*, *BC* and a cut *AB*. Point *D* is a reference location at the ground surface and the origin of the local one-dimensional coordinate *x* as shown in Fig. 1(a). It is noted that the distance of *DA* is defined as d. The intersection of lines *DA* and *CB* is the point *O*. The geometry of the wedge is characterized by 3 quantities, the length $|AB|=a$, right wedge angle $\angle AOB=\nu\pi$ and left wedge angle $\angle DAB=\nu_1\pi$. The corresponding wedge angle at B, $\angle ABC$, is then $\nu_1'\pi$, where $\nu_1'=\nu+(1-\nu_1)$. Thus, there are two cases of the wedge according to the values of ν_1 and ν_1'. When $\nu_1<\nu_1'$, the cut of the slope is shown in Fig. 1(a). When $\nu_1>\nu_1'$, the cut of the slope is gentle is shown in Fig. 1(b). In the following sections, the case of $\nu_1<\nu_1'$ will be discussed. In Fig. 1(a), two auxiliary quantities are defined for convenience as $|OA|=\dfrac{a\sin(\nu_1\pi-\nu\pi)}{\sin(\nu\pi)}=b$ and $|OB|=\dfrac{a\sin(\nu_1\pi)}{\sin(\nu\pi)}=c$, respectively.

The medium is assumed to be elastic, isotropic and homogeneous with shear modulus μ and density ρ, respectively. The harmonic SH wave excitations propagate with incident angle γ and circular frequency ω through the harmonic term $e^{-i\omega t}$. It has motions, *w*, in the (*out-of-plane*) *z*-direction perpendicular to the *xy*-plane. The time factor $e^{-i\omega t}$ will be assumed and omitted

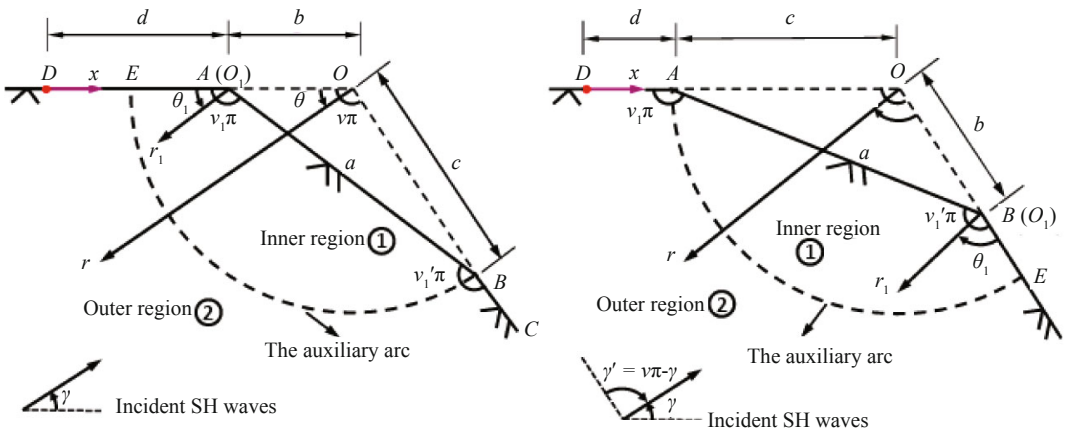

Fig. 1 The geometry of the proposed model

from all wave expressions in the following analysis. Here $i=\sqrt{-1}$ is the imaginary number.

In the formulation of the boundary-valued problem, an artificial, auxiliary arc method will be adopted. An auxiliary arc with the origin O and radius $|OB|$ is introduced to divide the slope on a wedged space into two regions, the inner and outer regions, as shown in Fig. 1(a). Two cylindrical coordinate systems are adopted in the model: the coordinate (r,θ) with origin at O and the coordinate (r_1,θ_1) with origin at O_1.

2.2 The Governing equations of the wave motions

For the steady-state excitations, the displacement w in the inner region ① and outer region ② each satisfies the Helmholtz wave equation as (Achenbach, 1973).

$$\left(\nabla^2 + k^2\right) w^{(j)} = 0 \tag{1}$$

where ∇^2 is the Laplace operator; $k = \omega/c$ is the wave number of SH waves in the medium; $c = c_s = \sqrt{\mu/\rho}$ is the shear wave speed (same in both regions); the superscript $j = 1, 2$ denotes the subregions of the inner ① and outer region ②, respectively.

The traction-free boundary conditions on the edge of the surfaces are, with $a = AB$, $b = OA$, $c = OB = OE$:

$$\tau_{\theta_1 z}^{(1)} = \frac{\mu}{r_1}\frac{\partial w^{(1)}}{\partial \theta_1} = 0 \quad (\theta_1 = 0,\ \nu_1\pi) \tag{2}$$

and

$$\tau_{\theta z}^{(2)} = \frac{\mu}{r}\frac{\partial w^{(2)}}{\partial \theta} = 0 \quad (\theta = 0,\ \nu\pi) \tag{3}$$

Along the artificial, auxiliary arc, the displacement continuity and stress balance are satisfied as

$$w^{(1)} = w^{(2)} \quad (r = c,\ 0 \le \theta \le \nu\pi) \tag{4}$$

$$\tau_{zr}^{(1)} = \tau_{zr}^{(2)} \quad (r = c,\ 0 \le \theta \le \nu\pi) \tag{5}$$

with $\tau_{zr}^{(1)} = \mu\dfrac{\partial w^{(1)}}{\partial r}$, $\tau_{zr}^{(2)} = \mu\dfrac{\partial w^{(2)}}{\partial r}$.

2.3 The total wave fields

2.3.1 The wave field in the outer region

The wave field $w^{(2)}$ in the outer region is written as a sum of the free field motion w^{f} and the scattered field w^{s} from the artificial, auxiliary arc using the coordinate system (r,θ) with origin at O:

$$w^{(2)}(r,\theta) = w^{\mathrm{f}}(r,\theta) + w^{s}(r,\theta) \tag{6}$$

The free field waves $w^{\mathrm{f}}(r,\theta)$ is (Eqs. (7), (8) & (9) are from Lee and Sherif, 1996 and Sherif and Lee, 1996)

$$w^{\mathrm{f}}(r,\theta) = \sum_{n=0}^{\infty} a_n J_{n/\nu}(kr)\cos\frac{n\theta}{\nu} \tag{7}$$

where $J_{n/\nu}(\cdot)$ is the Bessel function of the first kind with non-integer order n/ν; a_n is a set of input free-field coefficients expressed as

$$a_n = \frac{2}{\nu}\varepsilon_n e^{\frac{-in\pi}{2\nu}}\cos\frac{n\gamma}{\nu} \quad (n = 0,\ 1,\ 2\ldots) \tag{8}$$

where ε_n is the Neumann factor ($\varepsilon_0 = 1; \varepsilon_n = 2, n \ge 1$).

The scattered waves $w^{s}(r,\theta)$ from the auxiliary arc are represented as the out-going waves, for $0 \le \theta \le \nu\pi$

$$w^{s}(r,\theta) = \sum_{n=0}^{\infty} A_n H_{n/\nu}^{(1)}(kr)\cos\frac{n\theta}{\nu} \tag{9}$$

where $H_{n/\nu}^{(1)}(\cdot)$ denotes the Hankel function of the first kind with the same set of non-integer order n/ν; $A_n\ (n = 0,1,2\cdots)$ is the unknown complex coefficients to be determined.

2.3.2 The wave field in the inner region

Within the inner region, the motion is represented as standing waves $w^{(1)}(r_1,\theta_1)$ as, with respect to the coordinate system (r_1,θ_1) with origin at O_1:

$$w^{(1)}(r_1,\theta_1) = \sum_{l=0}^{\infty} B_l J_{l/\nu_1}(kr_1)\cos\frac{l}{\nu_1}\theta_1 \tag{10}$$

where B_l (l= 0, 1, 2 ...) is the unknown complex coefficients to be determined.

2.4 Solution of the boundary-valued problem

The unknown coefficients A_n and B_l are determined using the displacement and stress continuity conditions along the artificial, auxiliary arc. Equation (10) is first rewritten as

$$w^{(1)}(r_1,\theta_1) = \sum_{l=0}^{\infty} B_l\left[J_{l/\nu_1}(kr_1)\cos\frac{l}{\nu_1}(\theta_1-\theta)\cos\frac{l}{\nu_1}\theta - J_{l/\nu_1}(kr_1)\sin\frac{l}{\nu_1}(\theta_1-\theta)\sin\frac{l}{\nu_1}\theta\right] \tag{11}$$

In order to express the standing wave field $w^{(1)}$ in the inner region with respect to the coordinate system (r,θ), the Graf addition theorem is applied (Abramowitz and Stegun, 1972)

$$J_{l/\nu_1}(kr_1)\begin{Bmatrix}\cos\left[l/\nu_1(\theta_1-\theta)\right]\\ \sin\left[l/\nu_1(\theta_1-\theta)\right]\end{Bmatrix} = \sum_{m=-\infty}^{+\infty} J_{l/\nu_1+m}(kr)J_m(kb)\begin{Bmatrix}\cos(m\theta)\\ \sin(m\theta)\end{Bmatrix} \tag{12}$$

for $l=0,\ 1,\ 2\cdots$.

With the aid of Eqs. (11) and (12), the motion $w^{(1)}$ in the inner region in terms of the coordinate system (r,θ) is rewritten as:

$$w^{(1)}(r,\theta)=\sum_{l=0}^{\infty}B_l\sum_{m=-\infty}^{+\infty}J_m(kb)J_{l/\nu_1+m}(kr)\cos\left(l/\nu_1+m\right)\theta \tag{13}$$

Equation (13) can be expanded into Fourier cosine series of $(n\theta/\nu)$

$$w^{(1)}(r,\theta)=\sum_{n=0}^{\infty}\left[\sum_{l=0}^{\infty}B_l\sum_{m=-\infty}^{+\infty}c_{l,m,n}J_{l/\nu_1+m}(kr)\right]\cos\frac{n}{\nu}\theta \tag{14}$$

where for each $l,\ m,\ n=0,\ 1,\ 2\cdots$ and the Fourier coefficient $c_{l,m,n}$ is expressed as

$$c_{l,m,n}=\frac{\varepsilon_n}{\nu\pi}J_m(kb)\int_0^{\nu\pi}\cos\left(\frac{l}{\nu_1}+m\right)\theta\cos\frac{n}{\nu}\theta\mathrm{d}\theta \tag{15}$$

which can be evaluated in closed form as

$$c_{l,m,n}=\frac{\varepsilon_n}{\nu\pi}J_m(kb)\int_0^{\nu\pi}\cos\left(\frac{l}{\nu_1}+m\right)\theta\cos\frac{n}{\nu}\theta\mathrm{d}\theta$$
$$=\begin{cases}\dfrac{\varepsilon_n}{2\nu\pi}J_m(kb)\cdot\left\{\dfrac{\sin\left[\left(\dfrac{l}{\nu_1}+m+\dfrac{n}{\nu}\right)\nu\pi\right]}{\dfrac{l}{\nu_1}+m+\dfrac{n}{\nu}}+\dfrac{\sin\left[\left(\dfrac{l}{\nu_1}+m-\dfrac{n}{\nu}\right)\nu\pi\right]}{\dfrac{l}{\nu_1}+m-\dfrac{n}{\nu}}\right\}, & \text{if } \dfrac{l}{\nu_1}+m\neq\pm\dfrac{n}{\nu}\\ \varepsilon_n J_m(kb), & \text{if } \dfrac{l}{\nu_1}+m=\dfrac{n}{\nu}=0\\ \dfrac{\varepsilon_n}{2}J_m(kb), & \text{if } \dfrac{l}{\nu_1}+m=\pm\dfrac{n}{\nu}\neq 0\end{cases} \tag{16}$$

Considering the continuity conditions and substituting Eqs. (6) and (14) into Eqs. (4) and (5), a set of infinite linear equations of A_n and B_l is obtained, as for $n=0,\ 1,\ 2\cdots$

$$a_nJ_{n/\nu}(kc)+A_nH_{n/\nu}^{(1)}(kc)=\sum_{l=0}^{\infty}B_l\sum_{m=-\infty}^{+\infty}c_{l,m,n}J_{l/\nu_1+m}(kc) \tag{17}$$

$$a_nJ_{n/\nu}'(kc)+A_nH_{n/\nu}^{(1)}'(kc)=\sum_{l=0}^{\infty}B_l\sum_{m=-\infty}^{+\infty}c_{l,m,n}J_{l/\nu_1}'(kc) \tag{18}$$

where the prime denotes first derivative of the function.

Equations (17) and (18) constitute an infinite set of linear algebraic equations of the unknown coefficients A_n and B_l. This kind of infinite system should be resolved by truncating the series numbers n and l into the given value of N and m to $-M\sim+M$. The truncation is adopted according to the convergence and accuracy of the solution results. In addition, the values of N and M also depend on the parameters of interest given by d and harmonic frequency ω of the waves. In our experience, $N=10$ and $M=15$ are large enough for the convergence and accuracy of results for low frequency incidence when $d=2a$. However, terms n and m should be truncated as larger values for higher frequency, such as $N=30$, $M=35$ when $d=2a$.

2.5 General solution from the slope on a wedged space

The solution technique mentioned above is general and works not only on the case with gentle slope as shown in Fig. 1(a), but also on the case with steep slope in Fig. 1(b). The model in Fig. 1(b) can be transformed to that in Fig. 1(a) by a symmetrical transformation along the bisector of the angle $\angle AOB$. Thus, the incident angle γ needs to be replaced by $\gamma'=\nu\pi-\gamma$. After the transformation, the wave potential $w(x)$ along the ground surface in Fig. 1 is expressed as follows.

For the model in Fig. 1(a):

$$w(x)=\begin{cases}w^{(2)}(d+b-x,0), & (0\le x\le d+b-c)\\ w^{(1)}(d-x,0), & (d+b-c<x\le d)\\ w^{(1)}(x-d,\nu_1\pi), & (d<x\le d+a)\\ w^{(2)}(c+x-d-a,\nu\pi), & (d+a<x\le 2d+a)\end{cases} \tag{19}$$

For the model in Fig. 1(b):

$$w(x)=\begin{cases}w^{(2)}(d+c-x,\nu\pi), & (0\le x\le d)\\ w^{(1)}(d+a-x,\nu_1'\pi), & (d<x\le d+a)\\ w^{(1)}(x-d-a,0), & (d+a<x\le d+a+c-b)\\ w^{(2)}(x-d-a+b,0), & (d+a+c-b<x\le 2d+a)\end{cases} \tag{20}$$

3 Validation

Introduce three parameters, the motion amplitude $|w|$, the phase angle φ and the non-dimensional frequency η as

$$|w|=\sqrt{\mathrm{Re}^2(w)+\mathrm{Im}^2(w)} \tag{21}$$

$$\varphi=\tan^{-1}\left[\frac{\mathrm{Im}(w)}{\mathrm{Re}(w)}\right] \tag{22}$$

$$\eta=\frac{2a}{\lambda}=\frac{ka}{\pi} \tag{23}$$

where $\mathrm{Re}(\cdot)$ and $\mathrm{Im}(\cdot)$ denote the real and imaginary

parts of a complex variable, respectively; λ is the wave length of SH waves. η is the dimensionless frequency of thwaves.

The present method is verified by the surface motions of the wedged space (Sánchez-Sesma, 1985), as shown in Fig. 2. In the comparison, the angle $\nu_1\pi$ is assumed to equal to angle $\nu\pi$, so that the model is reduced to the wedged space without cut by a slope. It is seen that good agreement of the ground surface motions can be observed not only for low but also for high frequency waves. Moreover, a comparison is performed to validate the solution results with those by the finite element method as shown in Fig. 3. It is indicated from Fig. 3 that results by the proposed method agree also well with those by the finite element method. The FEM results, as shown in Fig. 3, were obtained by the commercial program ANSYS using rectangular mesh. The elements are modeled by the PLANE 83 elements in ANSYS. Two kinds of boundary conditions are set as: (1) All the in-plane translational degrees of freedom of the nodes are restrained; (2) The out-of-plane translational degree of freedom is restrained as well. The harmonic excitation is applied to the left edge of the analysis region. The size of mesh and the time step length were chosen carefully to guarantee the validity. For example, for higher frequency incidence of wave length $\lambda = 12$ m, the width of the mesh is selected as 1m and there are 30243 elements in analysis region. All the results are performed on a desktop computer with 3.70 GHz Intel dual-Core i3-6100 CPU and 4.00 GB RAM under Windows 7 64-bit OS envinment.

4 Surface motion in frequency domain

4.1 Effect of left wedge angle $\nu_1\pi$ and the incident angle γ

Figure 4 shows that the amplitudes and phases of surface motions for different topography left wedge angles $\nu_1\pi$ and incident angles γ under low incident frequency with $\eta = 0.4$. The wedge angle $\nu_1\pi$ varies from 120° to 180° representing different kinds of topography. It is seen that the surface motions are dependent greatly to the wedge angle $\nu_1\pi$ and the incident angle γ. For small horizontal and almost horizontal incidence such as $\gamma = 0$, 30° it is interesting that surface motions along the left part of the surface at $x/a \le 2$ are almost independent of the incident angles. However, the displacements along the right part $3 \le x/a \le 5$ are very sensitive to incident angles. When γ = 0, in Fig. 4(b), the motions decrease with increasing angle $\nu_1\pi$. A totally opposite trend can be observed for the motions along the right side ($3 \le x/a \le 5$) (Fig. 4(c)) for $\gamma = 30°$. This can be explained by the fact that the left ground surface is almost parallel to the propagating direction of the incident waves. Thus, surface motions on the left are almost identical to each other for cases of γ = 0, 30°. The right side of the ground surface, $3 \le x/a \le 5$, on the other hand, is facing the wave front of the incident waves. Therefore, the motion of the right surface is very sensitive to the directions of the incident waves.

For an incident angle of $\gamma = 60°$, quite an interesting phenomenon can be observed from Fig. 4(d). For the case of $\nu\pi = \nu_1\pi = 120°$, the point at $x/a = 2.5$ is located at the symmetry axis of the model under the incident angle of $\gamma = 60°$. Therefore, surface motion curve is symmetric about $x/a = 2.5$ as shown in Fig. 4(d). Moreover, for the case of $\nu_1\pi = 150°$, the propagating direction is perpendicular to the cut of the wedge. Thus, symmetrical curve is also observed along the midpoint of the cut for case of $\nu_1\pi = 150°$. With the increasing of the incident angle greater than $\gamma = 60°$, surface motion curves for γ = 90°, 120° are understood to be mirror images at $x/a = 2.5$ to those of γ = 30°, 0, respectively.

In addition to the wave propagation amplitude along the surface, the corresponding phase φ of surface motion normalized by π is plotted in Fig. 4. As shown in Figs.

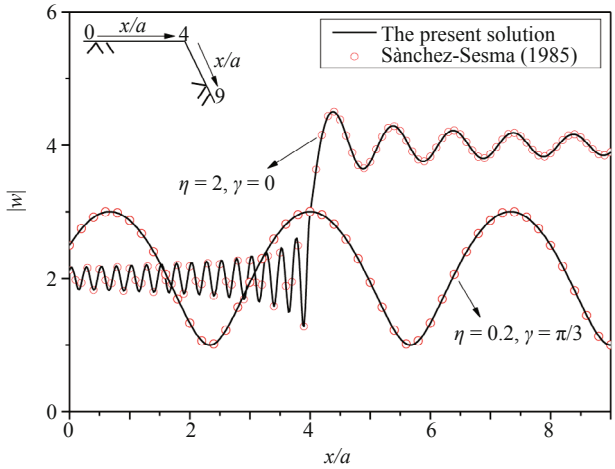

Fig. 2 Comparisons of the proposed solution results with those of Sánchez-Sesma (1985) ($d = 4a$, $v = 2/3$, $v_1 = 2.0001/3$, $N = 50$, $M = 50$)

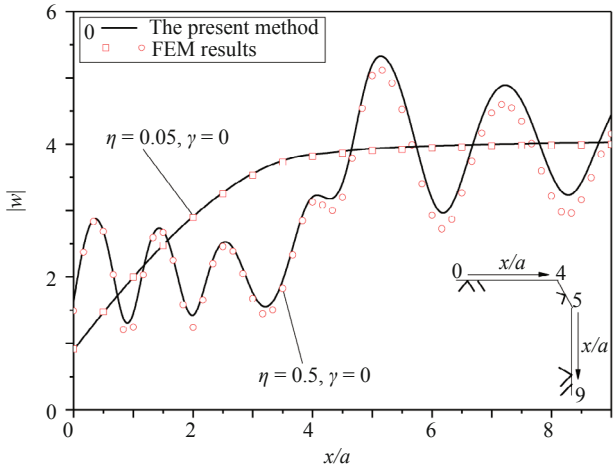

Fig. 3 Comparisons of the proposed solution results with FEM results ($d = 4a$, $v = 1/2$, $v_1 = 2/3$, $N = 50$, $M = 50$)

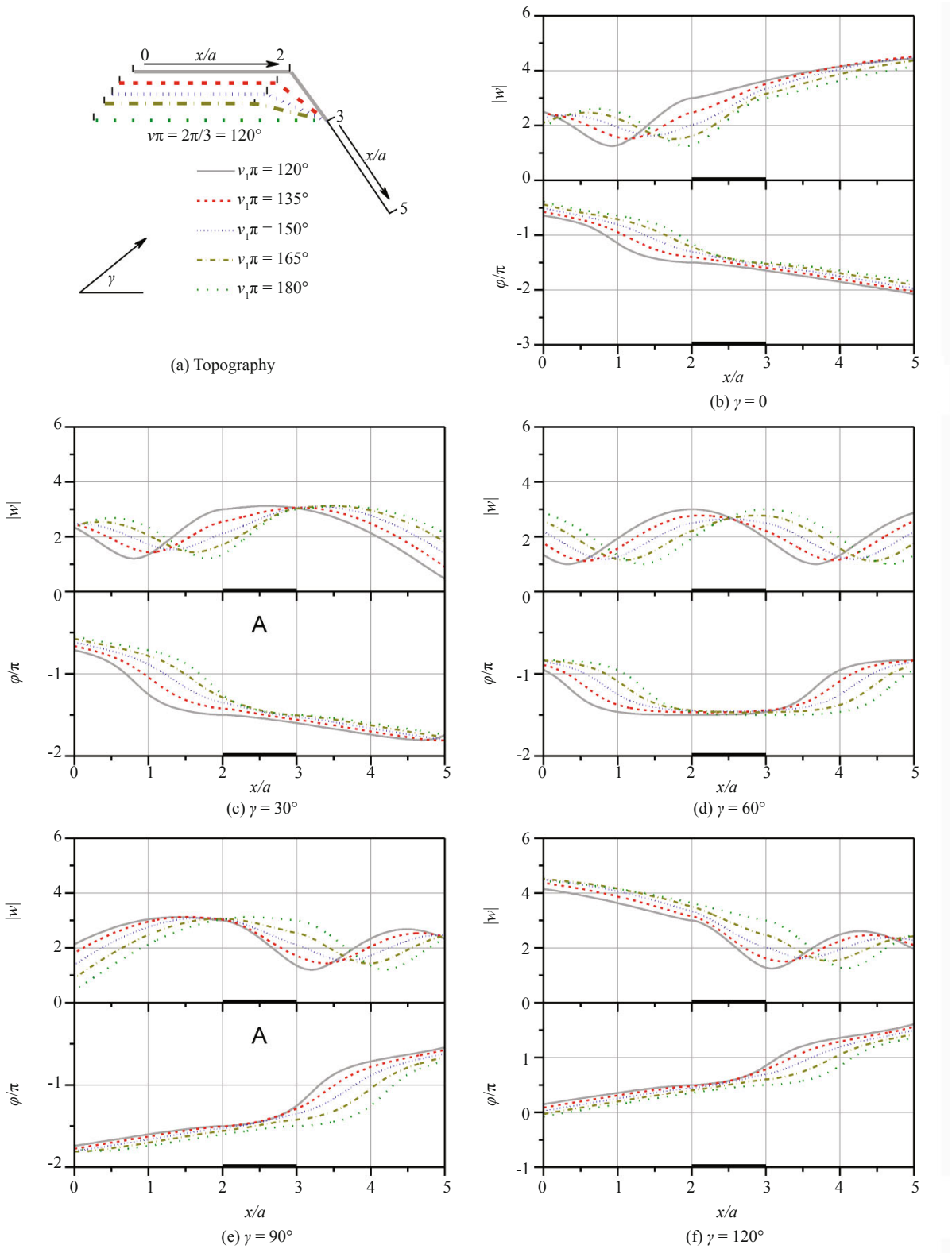

Fig. 4 Amplitudes and phases of surface motions at 5 selected left ($\nu_1\pi$), 1 right ($\nu\pi = 2\pi/3 = 120°$) topographical angles and 5 incident angles γ for small wave frequency ($\eta = 0.4$)

4(b) and 4(c), the phases for respective incident angles $\gamma = 0$, 30° have both negative slopes versus distance x/a representing the rightward wave propagation along the surface. However, the phases for incident angles $\gamma =$ 90°, 120° in Figs. 4(e) and 4(f), have the positive slopes versus x/a as the waves exhibit leftward propagation, reflecting from the right wedge surface is understood that the wave propagates from left to right if the incident

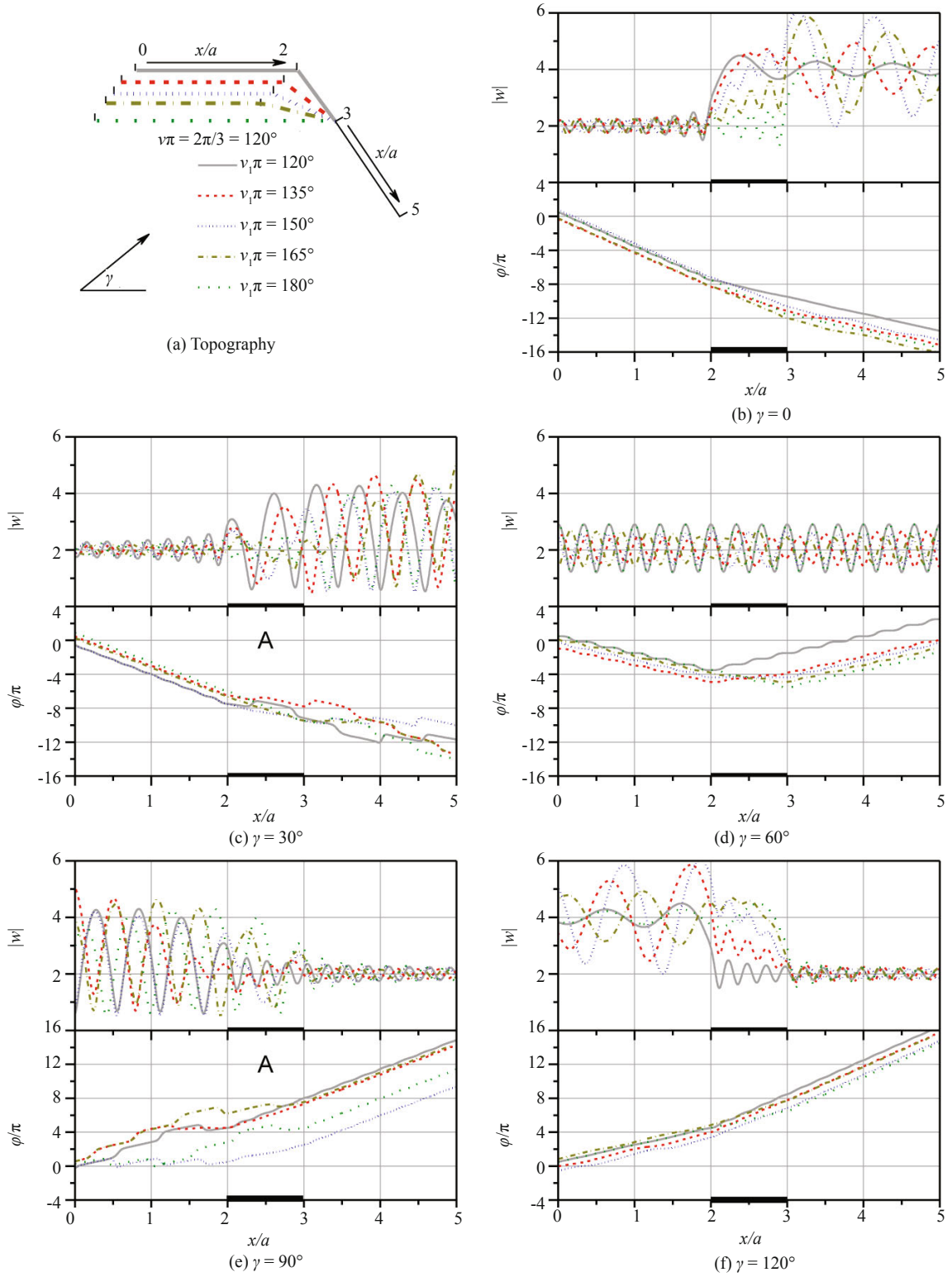

Fig. 5 Amplitudes and phases of surface motions at 5 selected left ($v_1\pi$), 1 right ($v\pi = 2\pi/3 = 120°$) topographical angles and 5 incident angles γ for large wave frequency ($\eta = 4.0$)

angle is very small. Meanwhile, if the incident angle is large, the wave front will instead meet the right side of the wedge first. It is also observed that the phases at the two edges of the wedge are equal (symmetrical) and greater than that in the center as shown in Fig. 4(d) for γ = 60°. This kind of phenomenon is consistent to that of the surface motions. It is also interesting when phase angle reaches $n\pi$, integer multiples of π, the corresponding surface motion approaches the peavalue.

Figure 5 shows the amplitudes and phases of surface

motions for different topography angle $\nu_1\pi$ and incident angle γ under high wave frequency with $\eta = 4.0$. It is shown in the figure that similar trend to Fig. 4 can be observed for surface motion except now the waves are much more oscillatory at high frequency. When the incident angle is small for $\gamma \le 30°$, the wave motions of the left edge of the wedge are smaller than that of the right side as indicated in Figs. 5(b) and 5(c). The waves from the left side will then interfere with the waves on the right. However, the wave motions on the left side are more intensive when the incident angle is greater. This can be understood that most part of the motion of the left side is due to the free field when the left side is almost parallel to the direction of the incident waves for small value of γ. This phenomenon can also be explained by the trend of the corresponding phase angles. It is seen that the phase angle φ decreases gradually with distance x/a for small γ. Thus, it is concluded that the left side of the wedge meets the wave front first. When $\gamma \ge 60°$, the wave front will stride both sides of the wedge simultaneously and the waves on the left side will now interfere with those from the right side, exhibiting larger oscillating mions.

4.2 Effects of the right wedge angle $\nu\pi$ and incident angle γ

Figure 6 shows the amplitudes and phases of surface motions with left-side wedge angle (at $x/a = 2$) at $\nu_1\pi$ = 150°, and for different topography with right-side wedge angles $\nu\pi$ = 90°, 120°, 150° and incident angles under low dimensionless wave frequency of $\eta = 0.4$. It is observed that motions along the left side $0 \le x/a \le 2$ of the wedge surface for waves with small incident angles $0° \le \gamma \le 45°$, are very similar in shape. The same is true for the motions along the right side $3 \le x/a \le 5$ of the wedge surface for waves with incident angles $60° \le \gamma \le 90°$. The corresponding phases of the surface motion are also shown in Fig. 6. It is seen that the phase angle decreases monotonously with increasing distance x/a for waves with small incident angles $0° \le \gamma \le 45°$. This means the wave front strikes the surface from the left to right successively. For waves with incident angle at $0\ \gamma \le 60°$, the waves are arriving at both sides of the wedge surfaces almost simultaneously, and hence the phase angles around $1 \le x/a \le 4$ are almost constant and is neither monotonically increasing or decreasing. For waves with larger incident angles beyond 60°, the wave front will now strike the surface from the right side towards the left side, so that the phases are now monotonically increasing from left to right.

One interesting feature Fig. 6 shows is the case of incident SH waves at right-side wedge angle of $\nu\pi$ = 90°, which means the right side surface is in the vertical direction. For waves with incident angles $0° \le \gamma \le 90°$ (cases Fig. 6(b-f)), the solid lines in Fig. 6 is the displacement motions for the case of $\nu\pi$ = 90°. It is seen that for each incident angle, the motions at one or two points along the wedge surfaces reach a minimum of an almost zero amplitude. The phase diagram in Fig. 6 shows that at these "nodal" points, the phases all have a jump of ±π, or a ±180° jump. It is at these points that the displacement is going in one direction on one side and in exactly the opposite direction on another side, hence apparently canceling the motion at the point, but exhibiting significant differential motions on each side and hence large rotational, torsional motion at these "nodal"oints.

Figure 7 shows the amplitudes and phases of surface motions again with left-side wedge angle (at $x/a = 2$) at $\nu_1\pi$ = 150°, and for different topography with right-side wedge angles $\nu\pi$ = 90°, 120°, 150° and incident angles now under higher dimensionless wave frequency of $\eta = 4.0$. As Fig. 7 shows, the motions, now at much higher frequency, is more oscillatory than those in Fig. 6. It is seen that, with decreasing right-side wedge angle from $\nu\pi$ = 150° down to $\nu\pi$ = 90°, the amplitudes of the motions increase. At $\nu\pi$ = 90°, where the right-side wedge surface is vertical, the (solid-line) motions range from almost zero to as high as four or above. As in Fig. 6, Fig. 7 now shows the corresponding phases of the surface motions in Fig. 7. The higher frequency waves now have the phases that cover the range of over 10π in the range $0 \le x/a \le 5$ shown.

Observe the solid curve in each of the five figures: Fig. 7(b) to 7(f). They are displacement motions along the wedge surface for the case $\nu\pi$ = 90°, the case of a quarter space for plane SH waves incident at γ = 0, 30°, 45°, 60°, 90°, respectively. It is noted that the displacement amplitudes of the solid line in each figure is significantly higher than the other two non-solid, dashed-line curves, which are the other two cases of wedge topography: $\nu\pi$ = 120° and $\nu\pi$ = 150°. It is known (Macdonald, 1902; Sherif and Lee, 1996) that in a 2-sided wedge space with wedge angle $\nu\pi$, the maximum free-field displacement amplification is $2/\nu$. Thus the three cases of $\nu\pi$ = 150°, 120°, 90°, or ν = 5/6, 2/3, 1/2, respectively in Fig. 7 will have a maximum free-field amplification of respectively 2.4, 3 and 4. This is consistent with the larger amplification amplitudes here for the case ν = 1/2, or $\nu\pi$ = 90°, the case of a quarter space. Thus it is observed that the solid lines in these figures for motions in a quarter-shaped wedge space have maximum amplitudes over four and minimum amplitudes of almost zero at some points. At points where the amplitudes are almost zero, the corresponding phases of these points in Fig. 7 show a jump of ±π or ±180°. At these points where the amplitudes are almost zero, the motions on each side of the point are ±180° different in phase, which means the motions are in opposite directions, creating a large rotational, torsional motions at these "nodal" points, which can cause significant damages, even though the motion is apparently zero there!

For other cases, we can make the same observations as that stated in Fig. 5.

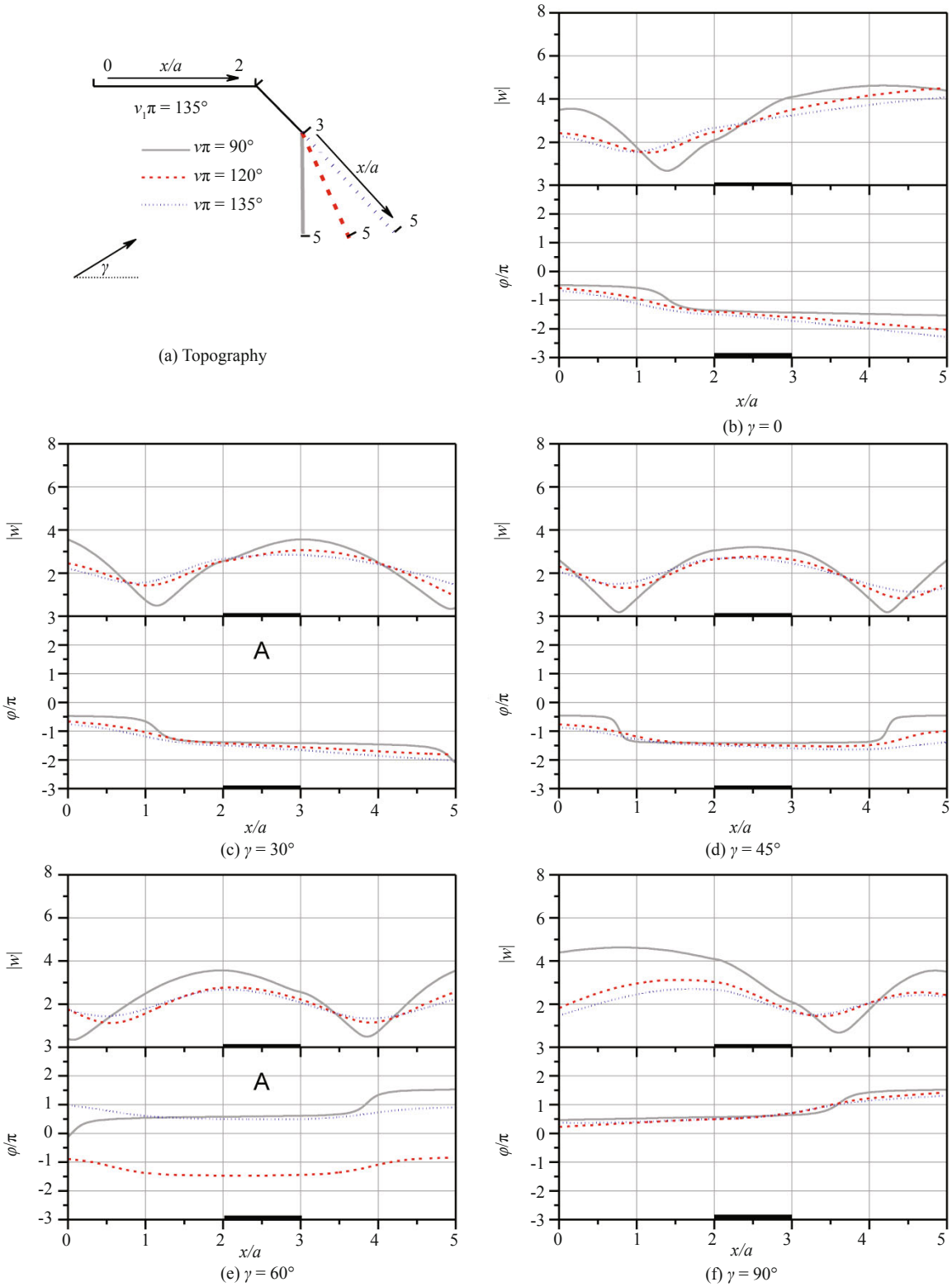

Fig. 6 Amplitudes and phases of surface motions at 1 selected left ($\nu_1\pi = 3\pi/4 = 135°$), 3 right ($\nu\pi$) topographical angles and 5 incident angles γ for small wave frequency ($\eta = 0.4$)

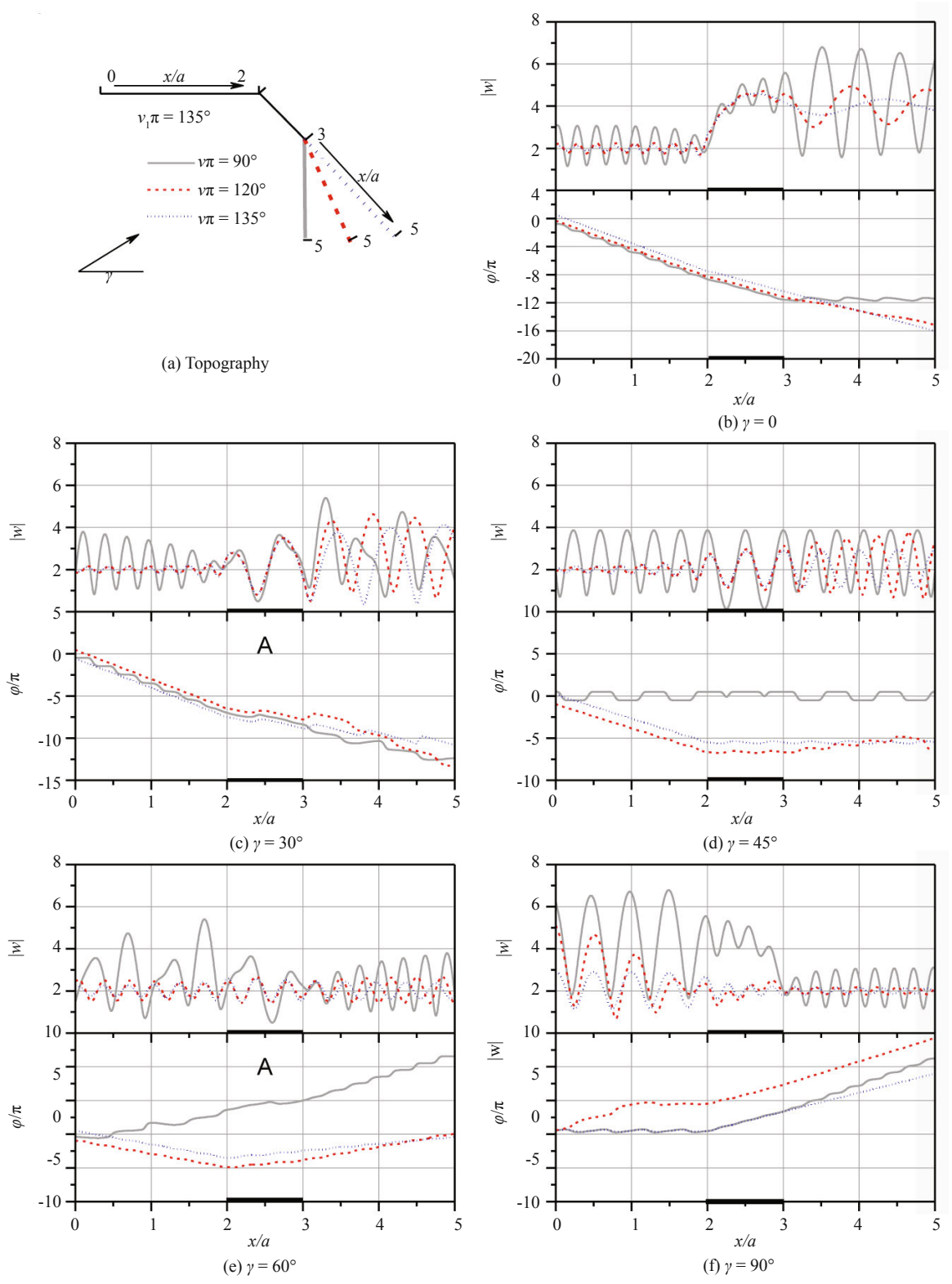

Fig. 7 Amplitudes and phases of surface motions at 1 selected left ($\nu_1\pi = 3\pi/4 = 135°$), 3 right ($\nu\pi$) topographical angles and 5 incident angles γ for large wave frequency ($\eta = 4.0$)

5 Conclusions

Surface motions of the slope on an elastic wedged space by SH plane wave excitations is investigated using the wave function expansion method. The domain of interest is divided into two subregions by an auxiliary arc. The wave potentials in the inner and outer regions are obtained using the separation-of–variables method. Graf addition theorem and Fourier series expansion are adopted to transfer the potentials in the inner sub-region.

The boundary-valued problem is formulated through the stress continuity and displacement continuity along the common interface of auxiliary arc. Some remarkable conclusions are drawn through numerical study:

1) The surface motion of the slope on a wedged space is influenced greatly by the topography, in particular, the wedge angles.

2) The topographic effect of the scattering of SH waves is negligible when the wavelength of the incident waves is large compared to the "size" of the wedge-cut shapes.

3) The phase decreasing in the direction along the surface coordinate is consistent to the SH waves propagating direction. Phase jumps of $\pm\pi$, or 180° are observed at points where the motions approach zero. These are points where the motions on either side are in opposite directions, resulting in significant rotational, torsional motions.

4) The surface motion approaches peak at the position where phase is at integer multiples of π.

References

Abo-Zena AM and King CY (1973), "SH Pulse in an Elastic Wedge," *Bull. Seismol. Soc. Am.*, **63**: 1571–1582.

Aboudi J (1971), "The Motion Excited by an Impulsive Source in an Elastic Half-Space with a Surface Obstacle," *Bull. Seismol. Soc. Am.*, **61**: 747–763.

Abramowitz M and Stegun IA (1972), *Handbook of Mathematical Functions, with Formulas, Graphs, and Mathematical Tables*, Dover, New York.

Achenbach JD (1973), *Wave Propagation in Elastic Solids*, North-Holland, Amsterdam.

Alielahi H, Kamalian M and Adampira M (2015), "Seismic Ground Amplification by Unlined Tunnels Subjected to Vertically Propagating SV and P Waves Using BEM," *Soil Dynam. Earthq. Eng.*, **71**: 63–79.

Amornwongpaibun A, Luo H and Lee VW (2016), "Scattering of Anti-Plane (SH) Waves by a Shallow Semi-Elliptical Hill with a Concentric Elliptical Tunnel," *J. Earthq. Eng.*, **20**: 363–382.

Bard PY (1982), "Diffracted Waves and Displacement Field over Two-Dimensional Elevated Topographies," *Geophys. J. Int.*, **71**: 731–760.

Boore DM (1972), "A Note on the Effect of Simple Topography on Seismic SH Waves," *Bull. Seism. Soc. Am.*, **62**: 275–284.

Bouchon M (1973), "Effect of Topography on Surface Motion," *Bull. Seism. Soc. Am.*, **63**: 615–632.

Bouchon M and Sánchez-Sesma FJ (2007), "Boundary Integral Equations and Boundary Elements Methods in Elastodynamics," *Adv. Geophys*., **48**: 157–189.

Chang K, Tsaur D and Wang J (2015), "Response of a Shallow Asymmetric V-Shaped Canyon to Antiplane Elastic Waves," *Philos. Trans. R. Soc. A.*, **471**: 20140215.

Fu L (2005), "Rough Surface Scattering: Comparison of Various Approximation Theories for 2D SH Waves," *Bull. Seism. Soc. Am.*, **95**: 646–663.

Gao Y and Zhang N (2013), "Scattering of Cylindrical SH Waves Induced by a Symmetrical V-Shaped Canyon: Near-Source Topographic Effects," *Geophys. J. Int.*, **193**: 874–885.

Gao Y, Zhang N, Li D, Liu H, Cai Y and Wu Y (2012), "Effects of Topographic Amplification Induced by a U-Shaped Canyon on Seismic Waves," *Bull. Seism. Soc. Am.*, **102**: 1748–1763.

Geli L, Bard PY and Jullien B (1988), "The Effect of Topography on Earthquake Ground Motion: A Review and New Results," *Bull. Seismol. Soc. Am.*, **78**: 42–63.

Hartzell SH, Carver DL and King KW (1994), "Initial Investigation of Site and Topographic Effects at Robinwood Ridge, California," *Bull. Seism. Soc. Am.*, **84**: 1336–1349.

Hough SE, Altidor JR, Anglade D, Given D, Janvier MG, Maharrey JZ, Meremonte M, Mildor BS-L, Prepetit C and Yong A (2010), "Localized Damage Caused by Topographic Amplification during the 2010 M 7.0 Haiti Earthquake," *Nature Geosci.*, **3**: 778–782.

Jeffery GB (1921), "Plane Stress and Plane Strain in Bipolar Co-ordinates," *Philos. Trans. R. Soc. London, Ser. A*, **221**: 265–223.

Lamé G (1859), *Lecons sur les Coordonnés Curvilignes*, Paris.

Le T, Lee VW and Trifunac MD (2016), "SH Waves in a Moon-Shaped Valley," *Earthq. Eng. Struct. Dyn.*, **101**: 162–175.

Lee VW (1990), "Scattering of Plane SH-Waves by a Semi-Parabolic Cylindrical Canyon in an Elastic Half-Space," *Geophys. J. Int.*, **100**: 79–86.

Lee VW, Luo H and Liang JW (2006), "Antiplane (SH) Waves Diffraction by a Semicircular Cylindrical Hill Revisited: an Improved Analytic Wave Series Solution," *J. Eng. Mech. ASCE*, **132**: 1106–1114.

Lee VW and Sherif RI (1996), "Diffraction Around Circular Canyon in Elastic Wedge Space by Plane SH-Waves," *J. Eng. Mech. ASCE*, **122**: 539–544.

Liu DK, Gai B and Tao G (1982), "Applications of the Method of Complex Functions to Dynamic Stress Concentrations," *Wave Motion*, **4**: 293–304.

Liu DK and Han F (1991), "Scattering of Plane SH-Wave by Cylindrical Canyon of Arbitrary Shape," *Soil Dyn. Earthq. Eng.*, **10**: 249–255.

Liu G, Chen HT, Liu DK and Khoo BC (2010), "Surface Motion of a Half-Space with Triangular and Semicircular Hills under Incident SH Waves," *Bull. Seism. Soc. Am.*, **100**: 1306–1319.

Liu Q, Zhang C and Todorovska MI (2016), "Scattering of SH Waves by a Shallow Rectangular Cavity in

an Elastic Half Space," *Soil Dyn. Earthq. Eng.*, **90**: 147–157.

Love AE 4th Edition, (1944), *A Treatise on the Mathematical Theory of Elasticity*, Dover, New York.

Luzón F, Sánchez-Sesma FJ, Rodriguez-Zuniga JL, Posadas AM, Garcia JM, Martin J, Romacho MD and Navarro M (1997), "Diffraction of P, S and Rayleigh Waves by Three-Dimensional Topographies," *Geophys. J. Int.*, **129**: 571–578.

MacDonald HM (1902), *Electric Waves*, Cambridge University Press, London, England.

Sánchez-Sesma FJ (1985), "Diffraction of Elastic SH Waves by Wedges," *Bull. Seism. Soc. Am.*, **75**: 1435–1446.

Sánchez-Sesma FJ and Campillo M (1991), "Diffraction of P, SV, and Rayleigh Waves by Topographic Features: A Boundary Integral Formulation," *Bull. Seism. Soc. Am.*, **81**: 2234–2253.

Sánchez-Sesma FJ and Rosenblueth E (1979), "Ground Motion at Canyons of Arbitrary Shape under Incident SH Waves," *Earthq. Eng. Struct. Dyn.*, **7**: 441–450.

Shah AH, Wong KC and Datta SK (1982), "Diffraction of Plane SH Waves in a Half-Space," *Earthq. Eng. Struct. Dynam.*, **10**: 519–528.

Sherif RI and Lee VW (1996), "Diffraction of a Circular Alluvial Valley in a Wedge Shaped Elastic Half Space due to Plane SH Waves," *Eur. J. Earthq. Eng.*, **10**: 21–28.

Sills LB (1978), "Scattering of Horizontally-Polarized Shear Waves by Surface Irregularities,"*Geophys. J. R. astr. Soc.*, **54**: 319–348.

Smith WD (1975), "The Application of Finite Element Analysis to Body Wave Propagation Problems," *Geophys. J. R. Astr. Soc.*, **42**: 747–768.

Sohrabi-Bidar A, Kamalian M and Jafari MK (2010), "Seismic Response of 3-D Gaussian-Shaped Valleys to Vertically Propagating Incident Waves," *Geophys. J. Int.*, **183**: 1429–1442.

Takemiya H and Fujiwara A (1994), "SH-Wave Scattering and Propagation Analyses at Irregular Sites by Time Domain BEM," *Bull. Seism. Soc. Am.*, **84**: 1443–1455.

Trifunac MD (1971), "Surface Motion of a Semi-Cylindrical Alluvial Valley for Incident Plane SH Waves," *Bull. Seism. Soc. Am.*, **61**: 1755–1770.

Trifunac MD and Hudson DE (1971), "Analysis of the Pacoima Dam accelerogram-San Fernando, California, earthquake of 1971," *Bull. Seism. Soc. Am.*, **61**: 1393–1141.

Trifunac MD (1973), "Scattering of Plane SH Waves by a Semi-Cylindrical Canyon," *Earthq. Eng. Struct. Dyn.*, **1**: 267–281.

Tsaur DH (2011), "Scattering and Focusing of SH Waves by a Lower Semi Elliptic Convex Topography," *Bull. Seism. Soc. Am.*, **101**: 2212–2219.

Tsaur DH and Chang KH (2008), "An Analytical Approach for the Scattering of SH Waves by a Symmetrical V-Shaped Canyon: Shallow Case," *Geophys. J. Int.*, **174**: 255–264.

Tsaur DH and Chang KH (2009), "Scattering and Focusing of SH Waves by a Convex Circular-Arc Topography," *Geophys. J. Int.*, **177**: 222–234.

Tsaur DH, Chang KH and Hsu MS (2010), "An Analytical Approach for the Scattering of SH Waves by a Symmetrical V-Shaped Canyon: Deep Case," *Geophys. J. Int.*, **183**: 1501–1511.

Wong HL and Jennings PC (1975), "Effects of Canyon Topography on Strong Ground Motion," *Bull. Seism. Soc. Am.*, **65**: 1239–1257.

Wong HL and Trifunac MD (1974), "Scattering of Plane SH Waves by a Semi-Elliptical Canyon," *Earthq. Eng. Struct. Dyn.*, **3**: 157–169.

Yuan X and Liao Z (1994), "Scattering of Plane SH Waves by a Cylindrical Canyon of Circular-arc Cross-Section," *Soil Dyn. Earthq. Eng.*, **13**: 407–412.

Yuan X and Liao Z (1996), "Surface Motion of a Cylindrical Hill of Circular-Arc Cross-Section for Incident Plane SH Waves," *Soil Dyn. Earthq. Eng.*, **15**: 189–199.

Yuan X and Men F (1992), "Scattering of Plane SH Waves by a Semi Cylindrical Hill," *Earthq. Eng. Struct. Dyn.*, **21**: 1091–1098.

Zhang C and Zhao C (1988), "Effects of Canyon Topography and Geological Conditions on Strong Ground Motion," *Earthq. Eng. Struct. Dynam.*, **16**: 81–97.

Zhang N, Gao Y, Cai Y, Li D and Wu Y, (2012), "Scattering of SH Waves Induced by a Non-Symmetrical V-Shaped Canyon," *Geophys. J. Int.*, **191**: 243–256.

Zhang N, Gao Y, Wu Y and Zhang F (2018), "A Note on Near-Field Site Amplification Effects of Ground Motion from a Radially Inhomogeneous Valley," *Earthq. Eng. Eng. Vib.*, **17**(4): 707–718.

Zhang C, Liu Q and Deng P (2017), "Surface Motion of a Half-Space with a Semicylindrical Canyon under P, SV, and Rayleigh Waves," *Bull. Seism. Soc. Am.*, **107**: 809–820.

Zhang C, Liu Q and Deng P (2015), "Antiplane Scattering of SH Waves by a Trapezoidal Valley with a Circular-Arc Alluvium in an Elastic Half Space," *J. Earthq. Tsunami*, **9**, Article ID 1550008.